Global mean sea level over the past 4.5 million years

Peter U. Clark^{1,2,†}, Jeremy D. Shakun^{3,†}, Yair Rosenthal^{4,5}, David Pollard⁶, Steven W. Hostetler¹, Peter Köhler⁷, Patrick J. Bartlein⁸, Jonathan M. Gregory^{9,10}, Chenyu Zhu¹¹, Daniel P. Schrag¹², Zhengyu Liu¹³, Nicklas G. Pisias¹

¹College of Earth, Ocean, and Atmospheric Sciences, Oregon State University, Corvallis, OR 97331

²School of Geography and Environmental Sciences, University of Ulster, Coleraine, Northern Ireland, UK BT52 1SA

³Department of Earth and Environmental Sciences, Boston College, Chestnut Hill, MA 02467

⁴Department of Marine and Coastal Science, Rutgers The State University, New Brunswick, NJ 08901

⁵Department of Earth and Planetary Sciences, Rutgers The State University, New Brunswick, NJ 08901

⁶Earth and Environmental Systems Institute, Pennsylvania State University, University Park, PA 16802

⁷Alfred-Wegener-Institut Helmholtz-Zentrum für Polar- und Meeresforschung, Bremerhaven, Germany

⁸Department of Geography, University of Oregon, Eugene, OR 97403-1251

⁹National Center for Atmospheric Science, University of Reading, Reading, UK

¹⁰Met Office Hadley Centre, Exeter, UK

¹¹Institute of Atmospheric Physics, Chinese Academy of Sciences, Beijing, China

¹²Department of Earth and Planetary Sciences, Harvard University, Cambridge, MA 02138

¹³Department of Geography, The Ohio State University, Columbus, OH 43210

*Correspondence to: clarkp@onid.orst.edu

†These authors contributed equally to this work.

This is the author's version of the work. It is posted here by permission of the AAAS for personal use, not for redistribution. The definitive version was published in *Science* on 16 October 2025, DOI: 10.1126/science.adv8389.

Link: https://www.science.org/doi/10.1126/science.adv8389.

Abstract

Changes in global mean sea level (GMSL) during the late Cenozoic remain uncertain. Here we use a new reconstruction of changes in $\delta^{18}O$ of seawater to reconstruct GMSL since 4.5 million years ago (Ma) that accounts for temperature-driven changes in the $\delta^{18}O$ of global ice sheets. Between 4.5 and 3 Ma, sea-level highstands remained up to 20 m above present while the first lowstands below present suggest onset of Northern Hemisphere (NH) glaciation at 4 Ma. Intensification of global glaciation occurred from 3 Ma to 2.5 Ma, culminating in lowstands similar to the Last Glacial Maximum lowstand at 21,000 years ago and that reoccurred throughout much of the Pleistocene. We attribute the middle Pleistocene transition in ice-sheet variability (1.2 Ma to 0.62 Ma) to modulation of 41-kyr obliquity forcing by an increase in ~100-kyr CO₂ variability.

The record of δ^{18} O measured in benthic foraminifera shells (δ^{18} O_b) (Fig. 1A) is widely used to represent the long-term evolution of combined changes in ocean temperature and global mean sea level (GMSL) over the Cenozoic (I-5) as well as to evaluate the response of the climate system to forcings on orbital and tectonic timescales (10^4 - 10^6 yr) (6-9). The fidelity of this record as a global signal has improved with the stacking of multiple records that increases the signal-to-noise ratio (10-12) and the use of several independent dating methods that provide a robust chronology (1, 11, 13, 14). Different strategies have then been used to decompose the δ^{18} O_b record into its temperature (δ^{18} O_T) and seawater (δ^{18} O_{sw}) components, with the former reflecting the temperature that the benthic foraminifera shells formed in (larger δ^{18} O_T in lower temperature) and the latter largely reflecting global ice volume (larger δ^{18} O_{sw} when more land ice). Although these strategies share the same goal, their different underlying assumptions have resulted in solutions with pronounced differences during the late Pliocene, early Pleistocene (beginning 2.6 Ma), and the middle Pleistocene transition (MPT) (defined herein as 1.2-0.62 Ma), thus confounding understanding of these critical periods of late-Cenozoic climate and GMSL change (fig. S1).

We address these issues by reconstructing GMSL for the past 4.5 million years (Myr) that circumvents several shortcomings associated with previous reconstructions (see supporting information, section 1). Using our new reconstruction of changes in global mean ocean temperature (Δ MOT), we previously decomposed a $\delta^{18}O_b$ stack (12) that includes a correction for some possible combination of diagenesis (15, 16) and the carbonate-ion effect on foraminifera (17) into its $\delta^{18}O_T$ and $\delta^{18}O_{sw}$ components (18). Here we convert our $\delta^{18}O_{sw}$ reconstruction (fig. S2C) to GMSL by applying a mass-balance approach that conserves $\delta^{18}O$ changes of the global ocean and the North American (Laurentide and Cordilleran) (NAIS), Eurasian (EUR), Greenland (GRN), and Antarctic (ANT) ice sheets, including loss of marine-based ANT ice (19, 20) (see the

supplementary materials, section 2). In doing so, our model accounts for time-varying temperature (21) and ice-volume effects on the $\delta^{18}O$ of ice sheets ($\delta^{18}O_i$) over the past 4.5 Myr that yields a variable relationship between $\delta^{18}O_{sw}$ and sea level (fig. S3), as opposed to methods that convert $\delta^{18}O_{sw}$ to sea level using a constant linear scaling between $\delta^{18}O_{sw}$ and sea level (22-26) or a variable scaling developed for just the last glacial cycle (27, 28).

Global mean sea level over the past 4.5 Myr

Our new reconstruction (Fig. 1C) shows that GMSL was largely above present from 4.5-4.0 Ma, with sea-level highstands of ~20 m and sea-level fluctuations of 5-20 m suggesting contributions likely from some combination of changes in GRN and ANT ice sheets although contributions from NAIS or EUR ice sheets cannot be excluded. Subsequent highstands between 4 and 3 Ma remained 15-20 m above present but lowstands now began to extend regularly below present by as much as -50 to -80 m thus marking the onset of extensive NH (NAIS, EUR) glaciation at ~4 Ma. The intensification of NH glaciation from 3 Ma to 2.5 Ma was marked by highstands that decreased to near-modern levels and lowstands that progressively decreased from -55±29 m at 3 Ma to -151±25 m at 2.52 Ma, which is comparable to or lower than the Last Glacial Maximum (LGM, 21 ka) lowstand (-132±15 m) (Fig. 1C). Since 2.5 Ma, sea-level highstands have been within +10 m of present except between 2.25 Ma to 1.45 Ma when they remained as much as 50 m below present, suggesting incomplete deglaciation of NH ice sheets, while fluctuations of large LGM-size ice sheets continued throughout the Pleistocene.

Three factors used to derive our GMSL reconstruction combine to indicate that early Pleistocene ice sheets were comparable in volume to the LGM in contrast to most previous reconstructions that suggest that such large ice sheets did not appear until after the MPT (fig. S6A-D). First, with a Δ MOT that is \sim 50% of a corresponding change in global mean sea surface

temperature (Δ SST) before the MPT (18), the increasing (cooling) trend of $\delta^{18}O_T$ is smaller in our reconstruction than if Δ MOT: Δ SST=1 is assumed throughout the Pleistocene. Being a residual from the observed $\delta^{18}O_{b}$, our $\delta^{18}O_{sw}$ is thus more negative during the Pliocene and has a larger increasing trend between 3.0-2.5 Ma (compare figs. S2A and S2B). Second, because ΔMOT:ΔSST was smaller during the early Pleistocene, so was glacial-interglacial MOT variability (15), limiting the contribution of $\delta^{18}O_T$ to glacial cycles in $\delta^{18}O_b$, in contrast to the middle and late Pleistocene when ocean temperature and ice volume exerted similar-size controls on δ^{18} O_b. Third, we find that higher global mean surface temperatures (GMST) during the early Pleistocene caused the ice sheets to be isotopically heavier (fig. S3D). This reduced their influence on $\delta^{18}O_{sw}$ relative to the isotopically lighter ice sheets during the middle and late Pleistocene. At the same time, given our reconstructed $\delta^{18}O_T$, Ref. (18) identified the need to remove a spurious increasing trend from the δ¹⁸O_b stack attributed to diagenesis (15, 16) or the carbonate-ion effect on benthic foraminifera (17) that, if unaccounted for, would have resulted in even more positive Pliocene $\delta^{18}O_{sw}$ values and larger early Pleistocene ice volumes than in our reconstruction (compare figs. S2B and S2C and figs. S2E and S2F).

The spectral characteristics of our GMSL reconstruction are dominated by 41-kyr variance until \sim 1.2 Ma. This is followed by the full emergence of a \sim 100-kyr signal by 0.62 Ma (Fig. 2A) representing the ice-sheet expression of the MPT. There have been similar concentrations of \sim 100-kyr and 41-kyr variance and a small concentration of 23-kyr variance over the past 0.8 Myr (Fig. 2A, 2B), with the latter being consistent with a long-term increase in precessional forcing from eccentricity modulation (29) rather than increasing southward expansion of NH ice-sheet margins during the MPT (30, 31). A 41-kyr filtered sea-level signal displays long-term (1 Myr) amplitude modulation of obliquity forcing until \sim 1 Ma, with lowest coherence between both occurring during

intervals of lower amplitude variations (i.e., nodes) (Fig. 2C, 2D). The increase in amplitude after the first node centered on 3.3-3.1 Ma may reflect a threshold response to the increase in obliquity forcing that led to the intensification of NH glaciation (32). The below-present highstands and reduced variability between 2.25 Ma and 1.45 Ma (Fig. 1F) are associated with the second node at ~1.8 Ma (Fig. 2C, 2D). The decrease in amplitude after the third node ~1 Ma reflects the decrease in size of 41-kyr ice sheets relative to those that characterized the Pleistocene prior to 1 Ma, with large ice sheets now occurring less frequently (every ~100 kyr) (Fig. 1C).

The evolution of changes in sea-level variability over the past 2.5 Myr as measured by sea-level terminations (defined as the maximum rate of sea-level rise during deglaciations) (Fig. 3D) shares the same relationship to obliquity as similarly defined GMST terminations (Figure 3B). This includes the occurrence of terminations between 2.5 Ma and 1.2 Ma for every (near-) maximum in obliquity, as previously found with an independent age model (*13*), except during the node in obliquity modulation centered on 1.8 Ma (Fig. 2C, 2D) when a small concentration of precessional variance appears (Figure 3F).

Over the past 1.2 Myr, we identify eight intervals (M8-M1) that begin and end with sealevel terminations associated with rising or peak obliquity (Fig. 3), with good agreement (within 0.5-4 kyr) between the mean ages of terminations during the past 1 Myr derived here and those derived from radiometric dating (14, 33, 34). Each of the eight intervals brackets 1-2 obliquity peaks without a corresponding termination (Fig. 3D, 3E), consistent with previous work (13, 35, 36). This low-frequency signal first appears at 1.19 Ma during the 72-kyr M8 interval. This pattern is repeated for the 78-kyr M7 interval between Terminations X (0.87 Ma) and IX (0.79 Ma) and the 89-kyr M6 interval between Terminations VIII (0.71 Ma) and VII (0.62 Ma), with each of these two intervals followed by a shorter length interval when a termination accompanies an obliquity

maximum. A similar interval of one skipped obliquity cycle between Terminations X and XII was inferred from a $\delta^{18}O_b$ record (*14*) but our $\Delta GMST$ and GMSL reconstructions show that the intervening Termination XI was as large as some earlier terminations (Fig. 3B, 3D). Five more intervals with 1-2 skipped obliquity cycles (M5-M1) span all of the past 0.53 Myr except for one brief 29-kyr interval between M3 and M2 (*34*) which reflects a temperature and sea-level oscillation during Marine Isotope Stage 7 associated with the strongest obliquity forcing since 2.5 Ma (Fig. 3C). The average duration of the M7-M1 intervals is 93.9±13.4 kyr, resulting in the "100-kyr cycle" seen in the late-Pleistocene spectra of $\Delta GMST$ and GMSL (Fig. 3F) and their rates of change (Figs. 3B, 3D). One notable difference is that GMSL terminations throughout the Pleistocene only occur after sea level falls below -80 m followed by the next increase to (near-) obliquity maxima (Fig. 3E), suggesting that ice sheets become unstable when exceeding this size, whereas GMST terminations have no comparable temperature threshold.

Our reconstruction of Pliocene highstands and the onset of NH glaciation between 4 and 3 Ma is in good agreement with other studies (37-39) including one that subtracted local temperature from $\delta^{18}O_b$ to derive $\delta^{18}O_{sw}$ and sea level as done here (40) (fig. S5). A similar local temperature-based reconstruction reproduces the intensification of NH glaciation that culminated in a LGM-like sea-level lowstand at ~2.5 Ma (26) (fig. S5) while another reproduces large ice sheets throughout the Pleistocene (41) (fig. S6E). To first order, the similarity between temperature-based sea-level reconstructions and our GMSL reconstruction is due to the local temperature reconstructions being nearly the same as our Δ MOT reconstruction (18). Several additional lines of evidence identify early Pleistocene NH ice sheets that were at or beyond their LGM extents by ~2.5 Ma, including well-dated terrestrial (42, 43), marine (44, 45), and geophysical (46) records

(Fig. 1D) and ice-rafted debris records in the North Atlantic (47) and North Pacific (48) oceans (Fig. 1E), consistent with them being volumetrically as large as at the LGM.

In contrast, changes in Pleistocene GMSL inferred from the $\delta^{18}O_b$ record (49, 50) (Fig. 1A) and from several reconstructions derived from it (9, 22, 25, 27, 28) find that the culminating lowstand at 2.5 Ma was only ~40% that of the LGM lowstand. Subsequent lowstands then remained at a similar intermediate level (~ -50 m) until the MPT when they furthered lowered, reaching LGM-like levels by 0.8 Ma (fig. S6A-D). Given the robust evidence for spatially extensive early Pleistocene ice sheets (Fig. 1D, 1E), the associated intermediate-size lowstands imply low-aspect ratio ice sheets relative to those following the MPT (i.e., on average thinner, since the ice volume is less but the area the same). This was the basis for the regolith hypothesis for the MPT (51). We attribute these findings of intermediate-size early Pleistocene ice sheets to the underlying methods that, by default, preserve the variability of the $\delta^{18}O_b$ record, including the increase in the size of glaciations during the MPT, with a further underestimation of early Pleistocene glaciations due to the lack of accounting for the long-term decrease in GMST on $\delta^{18}O_i$ (Fig. S3) (see the supplementary materials, section 1). Lastly, the good agreement between our reconstruction and all those that cover the past 0.8 Myr (fig. S7) suggest a robust understanding of GMSL since the MPT.

Towards resolving the paradox of large early Pleistocene ice sheets

A well-known paradox posed by early Pleistocene GMSL reconstructions is that their spectra are dominated by 41-kyr variability despite peak summer insolation being dominated by precession (52). Coupled climate and ice-sheet models have reproduced NH ice-sheet 41-kyr variability when accounting for albedo feedbacks, the integrated summer insolation forcing, and thin ice sheets with ablation zones that remained poleward of 60°N (36, 53, 54). However, such

ice sheets are inconsistent with the geologic evidence for their southern margins in North America reaching 39°N during the early Pleistocene (Fig. 1D) (42, 55) and they would not dominate the variability seen in our reconstruction. Another hypothesis proposes that higher early Pleistocene temperatures caused the response of the ANT ice sheet to precessional forcing to be out of phase with NH ice sheets, thus cancelling the 23-kyr signal in sea-level records (56). However, hemispheric Δ SST reconstructions show a dominant in-phase 41-kyr signal with virtually no precessional power (21) and this hypothesis cannot account for the large obliquity-driven NH ice sheets in our reconstruction which had about twice the volume as modeled by Ref. (56).

We propose that obliquity forced variations in the Southern Ocean carbon cycle during the early Pleistocene caused dominant [CO₂]_{atm} variability at this frequency (*57*). At the same time, the dominant 41-kyr signal of Southern Ocean SSTs and the temperature effects of related changes in the position of the sea-ice edge would have been advected through the shallow meridional circulation and upwelled in the equatorial Pacific (*58*, *59*), where they combined with the SST variability from CO₂ forcing to induce the observed dominant 41-kyr SST signal at these low latitudes (*21*, *60*). Observations (*61*) and modeling (*62*) show that changes in equatorial Pacific SSTs can strongly influence NH ice-sheet surface mass balance (SMB), with the ice-sheet changes then potentially acting as a positive feedback on equatorial Pacific SSTs (*63*).

Our results pose another dimension to this paradox in showing that large ice sheets existed throughout the Pleistocene while glacial GMSTs underwent a ~6°C long-term cooling (Figs. 1B, 1C), with polar amplification causing an even greater amount of cooling experienced by the high-latitude ice sheets (21). This relationship is further complicated by the strong effect that ice sheets have on their own local climate (64). We propose that the effects of higher early Pleistocene temperatures on ice-sheet SMB were mitigated by an associated increase in high-latitude

precipitation directly from warming (Clausius-Clapeyron relationship) as well as from latitudinal shifts in the westerlies as SST gradients changed (65). We can then infer that while cooling decreased accumulation over glaciated regions, the same cooling reduced surface ablation and thus caused SMB to remain positive. Similar transient relationships between other factors affecting SMB such as the influence of clouds on ice-sheet surface energy balance (66, 67) or terrestrial ecosystem emissions and atmospheric chemistry (68) can also be considered. If involved, changes in these transient feedbacks with global cooling continued to combine in such a way as to induce ice-sheet SMB that supported the growth of large ice sheets and then maintained their presence in response to obliquity forcing, suggesting an extraordinary balancing act that allowed the inception and growth of ice sheets to their maximum size under a range of GMST and [CO₂]_{atm}.

To explore this issue further, we conducted several experiments with the GENESIS V3.0 climate model (69, 70) to examine the sensitivity of early Pleistocene NH ice-sheet SMB to orbits, atmospheric CO₂, and ice-sheet height (see supporting information, section 4, Table S1). We first assessed our modeling strategy by running an experiment with LGM boundary conditions and found that the simulated NH ice sheets are in or have positive SMB. Our sensitivity experiments for early Pleistocene ice sheets included various combinations of orbits corresponding to low (at 2.165 Ma) and high (at 2.145 Ma) obliquity (71), [CO₂]_{atm} of 200 and 300 ppmv that covers much of the range suggested by proxies (72), and three ice-sheet configurations that assess sensitivity to ice-sheet height for a given LGM area (Table S1). Our results suggest that early Pleistocene ice sheets that were larger than LGM ice sheets could have been in SMB with low obliquity and [CO₂]_{atm} of 300 ppmv. SMB becomes more negative as ice-sheet height is lowered to LGM values unless there is a compensatory decrease in [CO₂]_{atm}. No decrease in [CO₂]_{atm} within the range of

our current understanding of its Pleistocene variability could support the low-aspect-ratio ice sheets in SMB inferred by the regolith hypothesis (51).

We thus conclude that the extra height of the early Pleistocene ice sheets relative to the LGM was critical to them being in SMB during glaciations. Given our finding that the large ice sheets shared a common size threshold throughout the Pleistocene equivalent to sea level below - 80 m that, when exceeded, triggered ice-sheet instabilities that culminated in a termination (Fig. 3E), we have narrowed this aspect of the paradox to understanding how different boundary conditions and feedbacks may have contributed to the inception and growth of the early Pleistocene ice sheets.

Towards resolving the paradox of the middle Pleistocene transition and the origin of the ~100-kyr cycle

The longstanding MPT paradox relates to the increase in amplitude and decrease in frequency of GMSL variability during the MPT in the absence of any corresponding change in orbital forcing (4). Our finding that large ice sheets existed throughout the Pleistocene, however, challenges several key aspects of their behavior that are usually invoked to explain this paradox: (i) that large ice sheets developed during the MPT in response to long-term changes internal to the climate system (4, 51, 73-78), (ii) that the time constant for growth of large ice sheets is significantly longer than for ice-sheet decay, giving rise to \sim 100-kyr cycles (79-81), and (iii) that through their large inertia and influence on climate, the large ice sheets drove the \sim 100-kyr cycle in the rest of the climate system (8, 82, 83).

We first note that because pre-MPT ice sheets were as large as those after the MPT, their albedo forcing should have remained largely the same throughout the Pleistocene and thus cannot explain the large increase in orbital-scale GMST variability during the MPT (Fig. 1B). Instead, we

attribute that increase to an increase in CO_2 variability associated with changes in the Southern Ocean carbon cycle. Ref. (21) proposed that the gradual cooling of the Southern Ocean through the early Pleistocene initiated the MPT in GMST at ~1.5 Ma when average extratropical Southern Hemisphere SSTs first decreased below pre-industrial, increasing the sensitivity of sea ice to the dominant obliquity forcing at these high latitudes. Increased cooling of the Southern Hemisphere also led to an equatorward shift of the westerly winds (84), an increase in dust flux to the Southern Ocean (85), and greater stratification of surface waters (86). Through their impacts on the Southern Ocean carbon cycle (84, 85, 87-90), these changes increased carbon storage during glaciations, thus increasing obliquity-scale variability of $[CO_2]_{atm}$ and GMST. However, a further decrease and then stabilization of Southern Ocean Δ SSTs at the end of the MPT in GMST ~0.8 Ma then muted the response of the Southern Ocean carbon cycle to obliquity forcing that may have dominated $[CO_2]_{atm}$ variability during the early Pleistocene, with an attendant large decrease in the concentration of 41-kyr variance in $[CO_2]_{atm}$ and GMST (21).

We similarly attribute the decrease in large-ice-sheet 41-kyr variance across the MPT (Fig. 2A, 2B) to modulation of obliquity forcing by the newly established decrease in [CO₂]_{atm} and GMST variance. Specifically, prior to reaching their maximum size at the end of each of the M intervals, ice-sheet response to low obliquity was modulated by periods of higher [CO₂]_{atm} and GMST, and vice versa, with times of maximum ice-sheet growth only occurring when the next obliquity low combined with low [CO₂]_{atm} and GMST (Figs. 4A, 4B, 4C). The initial retreat of large ice sheets in response to the next increase in obliquity then triggered a sequence of events and feedbacks leading to a termination every ~100 kyr (34). Among these feedbacks are large-ice-sheet instabilities that sustained ice-sheet retreat (8, 80, 91-94) which, through its influence on the Atlantic meridional overturning circulation, induced warming of the Southern Ocean with an

associated retreat of sea ice, deterioration of the Southern Ocean halocline, and poleward shift in the westerlies. These changes then led to the release of CO₂ from the deep ocean (90) which combined with obliquity (Fig. 4D) to fully deglaciate NH ice sheets and usher in the next interglaciation.

Contrasting temperature and ice-sheet responses to CO₂ forcing over the past 0.8 Myr are clearly expressed in their variance spectra, with a dominant ~100-kyr cycle in GMST (21) that is shared by CO₂ (fig. S9A) whereas the concentration of GMSL variance is nearly equally distributed between 41 kyr and ~100 kyr (Fig. 2B, fig. S9B). Insofar as the variance characteristics of GMST are shared by GMSST, MOT, and thus $\delta^{18}O_T$ (18) and those of GMSL are shared by $\delta^{18}O_{sw},$ we can similarly evaluate the relative contributions of $\delta^{18}O_{T}$ and $\delta^{18}O_{sw}$ to the variance of the $\delta^{18}O_b$ record since the MPT. The $\delta^{18}O_b$ record has long been used to argue that the dominant post-MPT ~100-kyr signal in that record (Fig. 5A) is from ice-sheet dynamics (8, 14, 95-97), but our results show that its origin is largely in the $\delta^{18}O_T$ component due to changes in the carbon cycle (Fig. 5B), as first recognized by Ref. (78). Overall, however, terminations present in both $\delta^{18}O_T$ and $\delta^{18}O_{sw}$ were set by the threshold of when ice sheets exceeded a limiting size beyond which they responded nonlinearly to obliquity forcing and helped drive a termination. This threshold was reached for nearly every obliquity cycle of the Pleistocene prior to the MPT (Fig. 3D, 3E). Afterward, the development of the ~100-kyr cycle arising from the long-term cooling enhanced the ability of the Southern Ocean carbon cycle to sequester CO2 and modulate the response of $\delta^{18}O_T$ and $\delta^{18}O_{sw}$ to obliquity forcing until the growth of the next large ice sheet.

Conclusions

We find that between 4.5 and 3 Ma, sea-level highstands remained ~20 m above present suggesting large decreases in AIS and GrIS volume relative to today. Beginning at 4 Ma, sea-level

lowstands began to episodically extend below present by as much as -50 to -80 m suggesting the onset of Northern Hemisphere (NH) glaciation. Sustained intensification of NH glaciation occurred from 3 Ma to 2.5 Ma, with highstands decreasing to near-modern levels while lowstands decreased to levels comparable to or lower than the Last Glacial Maximum (LGM) lowstand ~21 ka that continued throughout much of the Pleistocene.

Our finding that large ice sheets existed throughout the Pleistocene modifies as well as adds several fundamental challenges to our understanding of ice sheet-climate interactions and their joint responses to external forcing. Underlying each of these challenges is the fact that the dominant orbital-scale GMSL variability and its changes over the past 3 Myr is not the one that would be predicted solely by the associated orbital forcing, suggesting internal feedbacks of the climate system that we propose are largely driven by changes in the Southern Ocean carbon cycle and their effect on [CO₂]_{atm} and GMST. High-resolution ice-core CO₂ records that extend beyond 0.8 Ma are needed to test our hypotheses. Finally, the presence of large ice sheets throughout the MPT indicates that the hypothesis of regolith removal to explain the change in ice-sheet sensitivity to orbital forcing (5, 51) can be rejected.

Materials and Methods

Assessment of GMSL reconstructions

Two different approaches have been used to decompose the $\delta^{18}O$ record measured in benthic foraminifera ($\delta^{18}O_b$) into its two primary components: the temperature ($\delta^{18}O_T$) and the $\delta^{18}O$ of seawater ($\delta^{18}O_{sw}$) that the benthic foraminifera shells formed in, with the latter largely reflecting sea level. Ref. (24) developed an approach that regresses independently known sea-level data (e.g., from corals) on $\delta^{18}O_b$ for the last glacial cycle and then uses this regression to reconstruct sea level from $\delta^{18}O_b$ records for the last four glacial cycles. Sea level is then converted to $\delta^{18}O_{sw}$

using a constant relation of $\Delta\delta^{18}O_{sw}$: $\Delta GMSL$. Refs. (98) and (25) extended the regression over the last two glacial cycles to reconstruct sea level from $\delta^{18}O_b$ records over the last 5 Myr (figs. S1B, S6C). Refs. (27, 28) further extended the regression over the last 800 kyr using the LR04 $\delta^{18}O_b$ stack and a stack of sea-level records from Ref. (99) (fig. S7C) to reconstruct sea level over the last 40 Myr (figs. S1B and S6A show last 4.5 Myr). Refs. (27, 28) also accounted for $\delta^{18}O$ variations in land ice ($\delta^{18}O_i$) over the last glacial cycle which they then applied to their sea-level record to derive $\delta^{18}O_{sw}$ from $\delta^{18}O_b$, but this did not include the effect of increasing temperatures on $\delta^{18}O_i$ prior to 0.8 Ma. In any event, applying this regression approach to a $\delta^{18}O_b$ record will, by default, reproduce the variability of the $\delta^{18}O_b$ record, including the increase in the size of glaciations during the mid-Pleistocene transition (MPT), with the early Pleistocene low-amplitude variability further reinforced by not accounting for higher temperatures on $\delta^{18}O_i$.

Refs. (9) and (100) reconstructed sea level using a simple scaling relationship that determines the fraction of the LGM sea-level lowstand (-120 m in their case) from the fraction of the $\delta^{18}O_b$ value at any given time relative to the LGM $\delta^{18}O_b$ value. As with the regression method, this relationship reproduces the $\delta^{18}O_b$ variability throughout the Pleistocene as well as does not account for the effect of increasing temperatures on $\delta^{18}O_i$ prior to 0.8 Ma, resulting in smaller early Pleistocene ice sheets than in our reconstruction (figs. S1B, S6D). Finally, these approaches imply a stationary partitioning of $\delta^{18}O_b$ between temperature and ice volume, and thus do not capture the larger ice volume component relative to temperature that we identify before the MPT (18).

Another approach that is similar to ours subtracts independently reconstructed seawater temperature as $\delta^{18}O_T$ from $\delta^{18}O_b$ to derive $\delta^{18}O_{sw}$ (22, 23, 41, 101-103) which can then be converted to GMSL using a relation of $\Delta\delta^{18}O_{sw}$: Δ GMSL (22, 23). Ref. (22) used a reconstruction of bottom water temperature (BWT) that is similar to ours in showing lower Δ BWT than Δ SST

during the early Pleistocene (18). However, this is a 2-Myr smoothed record and thus does not capture the increase in orbital variability across the MPT (18) (figs. S1B, S6B) which contributes to larger early Pleistocene ice sheets in our reconstruction. Ref. (22) also applied a constant 0.013% m⁻¹ relationship to derive sea level from their $\delta^{18}O_{sw}$ which does not account for the effect of warmer early Pleistocene temperatures on $\delta^{18}O_{i}$, and thus $\delta^{18}O_{sw}$. Moreover, this relationship is more appropriate for warmer climates with just the Greenland and Antarctic ice sheets (19) as opposed to the 0.008% m⁻¹ relationship that is more suitable for deriving sea level after 0.8 Ma. Accordingly, their sea-level lowstands are generally higher than in our reconstruction throughout the Pleistocene (figs. S6B, S7B).

Other studies that used independent orbital-scale temperature records to derive $\delta^{18}O_{sw}$ from $\delta^{18}O_b$ suggest small GMSL variability in the late Pliocene that increases into the early Pleistocene and continues across the MPT (26, 40, 41). We used our method to convert $\delta^{18}O_{sw}$ data from Refs. (41) and (26) to sea level (see section 2 of this Supplementary Materials) and find generally good agreement with our GMSL reconstruction (figs. S5, S6E). However, the temperature records in Refs. (41) and (26) are local and so may not be representative of mean ocean temperature (MOT). Finally, other than Refs. (27) and (28), none of the reconstructions using either approach account for changing $\delta^{18}O_i$ on $\delta^{18}O_{sw}$ (28, 104).

Finally, Refs. (105, 106) reconstructed changes in water depth using grain size variations in uplifted marine sedimentary sequences preserved in New Zealand (fig. S1, S8), with inferred water depths being supplemented by estimates from benthic foraminifera. Unconformities in the sedimentary sequence are assigned a maximum water depth of -32.5 m, and the authors assume the missing part of the sea-level record to be <5 m. Water depth is converted to relative sea level using back stripping methods that account for sediment compaction and tectonic subsidence. Their

reconstruction cannot be referenced to Holocene sea level, but it does identify long-term trends as well as the frequency and amplitude of sea-level change on orbital timescales. Comparison of their reconstruction to other sea-level reconstructions (fig. S1) and to our reconstruction (fig. S8) shows a similar concentration of 41-kyr variance but disagrees with these other reconstructions in showing no trend of increasing lowstands (i.e., greater amplitude) during the intensification of Northern Hemisphere glaciation.

Conversion of $\delta^{l8}O_{sw}$ to sea level

We develop a simple model to translate $\delta^{18}O_{sw}$ to sea level that conserves global water and ^{18}O mass as they are redistributed between the ocean and the North American (NAIS) (Laurentide and Cordilleran ice sheets), Eurasian (EUR), Greenland (GRN), and Antarctic (ANT) ice sheets. The model also accounts for the changing isotopic composition of each ice sheet through time as a function of changes in its volume and global temperature, which allows us to separate their isotopic effects. This is important because our reconstructions suggest that there is not a constant scaling between global temperature and ice volume over the past 4.5 Myr.

The method is based on conservation of global water and isotopic ¹⁸O mass, extending similar treatments in Ref. (19) and Ref. (20). A simple expression is used for the mean δ^{18} O of each ice sheet as a linearized function of its size and global mean surface temperature (GMST), and a parameterization is assumed for the relative size of each ice sheet to the others at all times. After some tedious but straightforward algebra, this yields a quadratic equation yielding total ice volume over flotation (and hence global sea-level rise) as a function of δ^{18} O_{sw} and GMST.

While $\delta^{18}O_{sw}$ is often converted to sea level using a constant scaling of ~-0.008 %/m based on Last Glacial Maximum values (i.e., a ~1 % $\delta^{18}O_{sw}$ enrichment (107) and ~130 m sea level lowering (108)), our model accounts for time-varying temperature and ice-volume effects on ice-

sheet $\delta^{18}O_i$ (fig. S3D), yielding a variable relationship between $\delta^{18}O_{sw}$ and sea level (fig. S3A, S3B). As a result, relative to linear scaling, applying our model to our $\delta^{18}O_{sw}$ reconstruction produces lower sea levels during early Pleistocene glaciations because less-negative $\delta^{18}O_{ice}$ then (due to higher temperatures) requires greater ice growth to explain $\delta^{18}O_{sw}$ enrichments, and thus lower sea levels during Pliocene interglaciations because more-negative $\delta^{18}O_{ice}$ then (due to NAIS and EIS absence) requires less ice loss to explain $\delta^{18}O_{sw}$ depletions (fig. S3A).

In the Supplementary Materials, we explain the details of our model. Section 1 derives separate equations for differing climates relative to today. Section 2 outlines how we estimate the coefficients in the expression for mean ice-sheet $\delta^{18}O$ based on observed quantities and published general circulation model (GCM) experiments. Section 3 explains the scheme we use to account for the residence time of ice in each ice sheet, and a list of prescribed quantities is given in section 4. Finally, section 5 assesses the sensitivity of our sea-level reconstruction to the various parameters in our model. Finally, section 6 provides the MATLAB code for converting $\delta^{18}O_{sw}$ to sea level.

Time series analyses

We characterized the temporal variability and covariability of the different time series in four ways, using: 1) evolutionary spectra (Fig. 2A); 2) "global" multitaper spectral analysis (Fig. 2B); 3) bandpass-filtered time series of ΔGMST and SL at the 41 kyr obliquity period (Fig. 2C); and 4) the rolling coherence between the filtered series and obliquity (Fig. 2D). Evolutionary spectra (109) were calculated using the R astrochron package (110, 111). The function eha() in the astrochron package implements a moving-window application of the multi-taper method (MTM) spectral-analysis procedure (112). We used a window width of 500 kyr, a time step of 10 kyr between adjacent window positions, and a "standard" MTM time-bandwidth product of 4. Prior to

analysis, the time series were detrended using a smoothing spline with 10 degrees of freedom using the spline.smooth() function in the R base stats package (III). This detrending step removes the very long-period variability from the time series but does not obscure or overly emphasize the eccentricity band variations in the data. The spectral density was rescaled to "normalized amplitude" values—in each window, the amplitudes (the square root of the spectral density) at each frequency were divided by the maximum amplitude across all frequencies. This facilitates judging the relative importance of variations across periods. We did not do any significance testing of the results because the presence of variability in the time series at orbital frequencies is really not in question, and white-noise or low-order autoregressive null-hypothesis spectra are rather naïve. On Fig. 2A, the dominant periods in insolation variations at orbital periods are indicated by horizontal lines (eccentricity: $E_1 = 400 \text{ kyr}$, $E_2 = 96 \text{ kyr}$; obliquity: T = 41 kyr and precession: $P_1 = 23 \text{ kyr}$, $P_2 = 19 \text{ kyr}$).

Global (as opposed to evolutionary) spectral analysis was performed for blocks of data, as indicated by the black horizontal bars on Fig. 2A. We used the multitaper method here as well. We bandpass-filtered the time series at the 41 kyr obliquity period using the butter() (Butterworth filter) function from the R signal package (113). The band limits were 39.0 and 43.1 kyr, 0.95 and 1.05 times the obliquity frequency of 1/41.0 = 0.0244 cycles kyr⁻¹. The coherence between obliquity and ΔGMST and SL was calculated using a moving window approach. Cross-spectral analyses were done following the Blackman-Tukey method using the SPECTX2 function from the ARAND software package (114). The number of lags used correspond to ~1/3 the length of the interval analyzed.

Ice-sheet surface mass balance

We assessed the sensitivity of the surface mass balance (SMB) of early Pleistocene Northern Hemisphere ice sheets to orbits, atmospheric CO₂, and ice-sheet height by conducting experiments with the GENESIS V3.0 climate model (69, 70) (Table S1). The GENESIS climate model comprises a T31 atmospheric model (horizontal resolution of approximately 3.75° × 3.75° latitude by longitude) coupled with the land-surface model LSX (2° × 2° resolution). SSTs were computed by the 50-meter mixed layer ocean model in GENESIS. SMB is computed from annual precipitation, runoff, and evaporation over the ice sheets on the 2° ×2° grid of the LSX land surface model. The fraction of runoff retained through refreezing is computed as a function of temperature and precipitation using the method of Ref. (115). We ran the simulations for 100 years and analyzed the last 70 years to exclude spin-up artifacts.

Our sensitivity experiments used orbits corresponding to low (glacial) and high (interglacial) obliquity at 2.165 Ma and 2.145 Ma (71), respectively, and atmospheric CO₂ values of 200 and 300 ppmv which cover much of the early Pleistocene range suggested by proxies (57, 116, 117). We used three ice-sheet configurations to assess sensitivity to ice-sheet height for a given LGM area (Table S1). The GLAC-1D LGM ice sheets are from Ref. (118). The HIGH ice sheets are intended to represent the largest of the early Pleistocene ice sheets, with ~30 m of additional lowering of sea-level relative to the LGM sea-level lowstand (Figs. 1C, 3E). We derived the HIGH ice-sheet heights by calculating the volume of 30 m of global sea level and distributing the height equivalent of the volume uniformly over the GLAC 1-D LGM North American (NA) (20 m) and Eurasian (EU) (10 m) ice-sheet complexes, accounting for the density ratio of water to ice (1028 kg m⁻³/910 kg m⁻³). The LOW ice sheet was derived by reducing the GLAC 1-D LGM ice-sheet height to an equivalent of 60% of the full LGM sea-level volume and is intended to represent the low-aspect ratio ice-sheet geometry inferred from the regolith hypothesis (51).

Experiment EXP1 shows the model's ability to simulate NH (GLAC-1D) ice sheets that are in SMB or have positive SMB under LGM boundary conditions (Table S1). Experiments EXP2 and EXP3 assess the effect of orbital changes on NH ice-sheet SMB (Table S1). In both experiments, NH MATs north of 40°N are 8 K to 9 K colder than the PI due to the presence of the ice sheets while North Atlantic SSTs are 3 K to >5 K colder due to advection of cold air off the NA ice-sheet complex and southward expansion of sea ice (fig. S10A). Warming of the oceans elsewhere partially offsets the NH cooling such that global SSTs are the same as PI and global MATs are 2 K colder than PI (Table S1). The net effect of the boundary conditions yields a glacial NA ice-sheet-complex SMB of 5 m yr⁻¹ (fig. S10B) and an interglacial SMB of -11 m yr⁻¹. Comparison of the NA and EU ice-sheet-complex SMB in EXP2 to that of EXP3 indicates that glacial-interglacial obliquity accounts for 16 m yr⁻¹ over NA and 2 m yr⁻¹ over EU (Table S1, fig. S10C).

Experiments EXP2 and EXP4 assess the effect of CO₂ changes on NH ice-sheet SMB. Over the 200 to 300 ppm range evaluated here, CO₂ accounts for 15 m yr⁻¹ in the NA ice-sheet complex SMB and 8 m yr⁻¹ in the EU ice-sheet complex SMB, which are comparable to the effect of obliquity (Table S1). Experiments EXP2 and EXP5 and experiments EXP4 and EXP6 assess the effect of ice-sheet height on NH ice-sheet SMB (Table S1). Lowering the ice-sheet height from HIGH (EXP2) to GLAC-1D (EXP5) results in SMB becoming more negative by 35 m yr⁻¹ for the NA ice-sheet complex and 11 m yr⁻¹ for the EU ice-sheet complex (Table S1). The effect of height on mass balance is most evident along the margin of the NA ice-sheet complex (fig. S10D) where the higher margin blocks penetration of precipitation into the interior (orographic shadowing) and positions more ice area at or above the zero-degree isotherm. The marginally more positive SMB

over the interior of the NA ice-sheet complex for the lower ice sheet where precipitation is slightly greater than that of the high ice sheet reflects the effect of desertification.

Lowering the ice sheet from HIGH (EXP4) to LOW (EXP6) results in SMB becoming more negative by 84 m yr⁻¹ for the NA ice-sheet complex and by 4 m yr⁻¹ for the EU ice-sheet complex (Table S1). We note that the strongly negative SMB of the LOW ice sheet in EXP6 (Table S1) indicates that such an ice sheet could not have existed even under glacial orbitals and LGM CO₂ levels.

In summary, our sensitivity tests suggest that early Pleistocene ice sheets that were larger than LGM ice sheets could have been in SMB with low obliquity and CO₂ levels of 300 ppm. SMB becomes more negative as ice-sheet height decreases towards LGM values unless there is a compensatory decrease in CO₂, but no decrease in CO₂ within the range of our current understanding of its Pleistocene variability could support the low-aspect-ratio ice sheets in SMB inferred by the regolith hypothesis (51). We note that while our experiments using LSX and a mixed layer ocean model are a first-order assessment of the sensitivity of ice-sheet SMB to changes in boundary conditions, the model does not account for feedbacks such as changes in global ocean circulation and ice-sheet dynamics that, when investigated with a full Earth System model, would further refine our results. The challenge remains for modeling the inception and growth of the ice sheets.

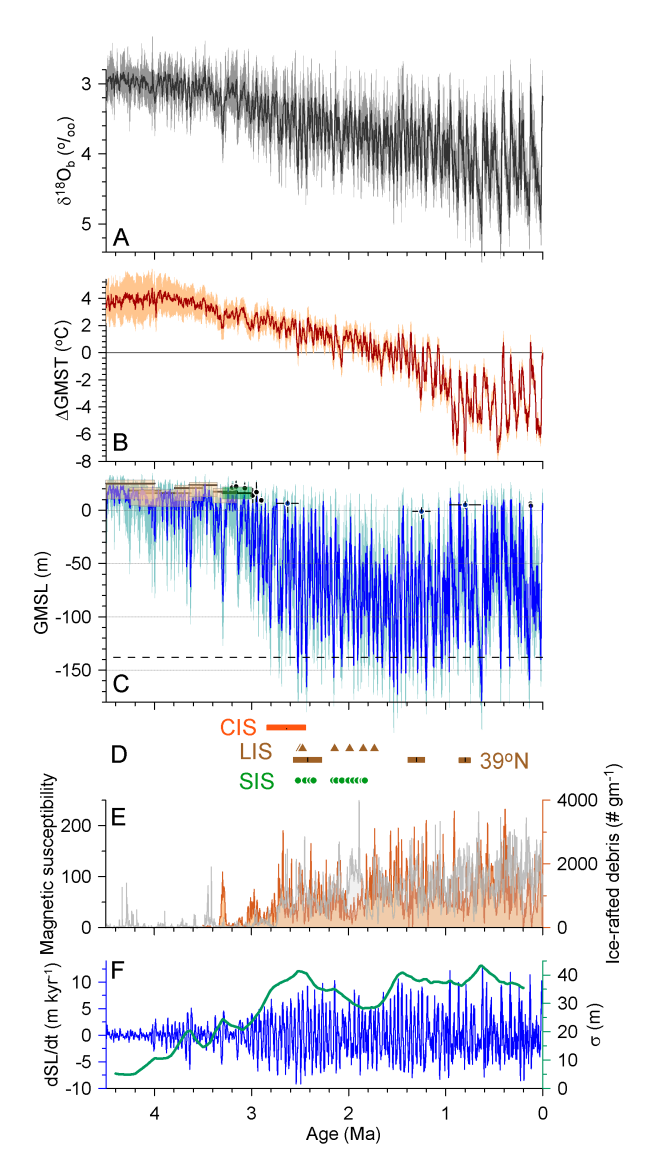


Fig. 1. Global mean temperature and sea-level changes over the past 4.5 Myr. (A) Prob-stack δ^{18} O_b record (12). (B) Global mean surface temperature difference (ΔGMST) (brick red with 1σ uncertainty) referenced to PI. (C) Global mean sea level (GMSL) (blue line with 1σ uncertainty). The uncertainty on δ^{18} O_{sw} (converted to sea level) is calculated as the square root of the sum of squares of the uncertainty in the Prob-stack δ^{18} O_b record (12) and in the ΔMOT reconstruction (as δ^{18} O) (18). Also shown are published Pliocene (37-39) and Pleistocene (119, 120) sea-level highstands. Dashed horizontal line is referenced to the LGM lowstand (-130 m). (D) Geologic evidence of extensive margins of early-to-middle Pleistocene Cordilleran Ice Sheet (CIS, orange symbols) (43), Laurentide Ice Sheet records at 39°N (LIS, brown symbols) (42, 44), and Scandinavian Ice Sheet (SIS, green symbols) (46). Newer evidence suggests a more-limited extent of the SIS in the North Sea prior to 1.1 Ma (121) than inferred by Ref. (46), but the difference in extent, and its contribution to GMSL, is negligible. (E) Records of ice-rafted debris from the North Pacific (gray) (48) and Nordic Seas (orange) (47). (F) Rate of change (12-kyr running average) (dark blue line) and standard deviation (σ, 200-kyr centered) (green line) of GMSL.

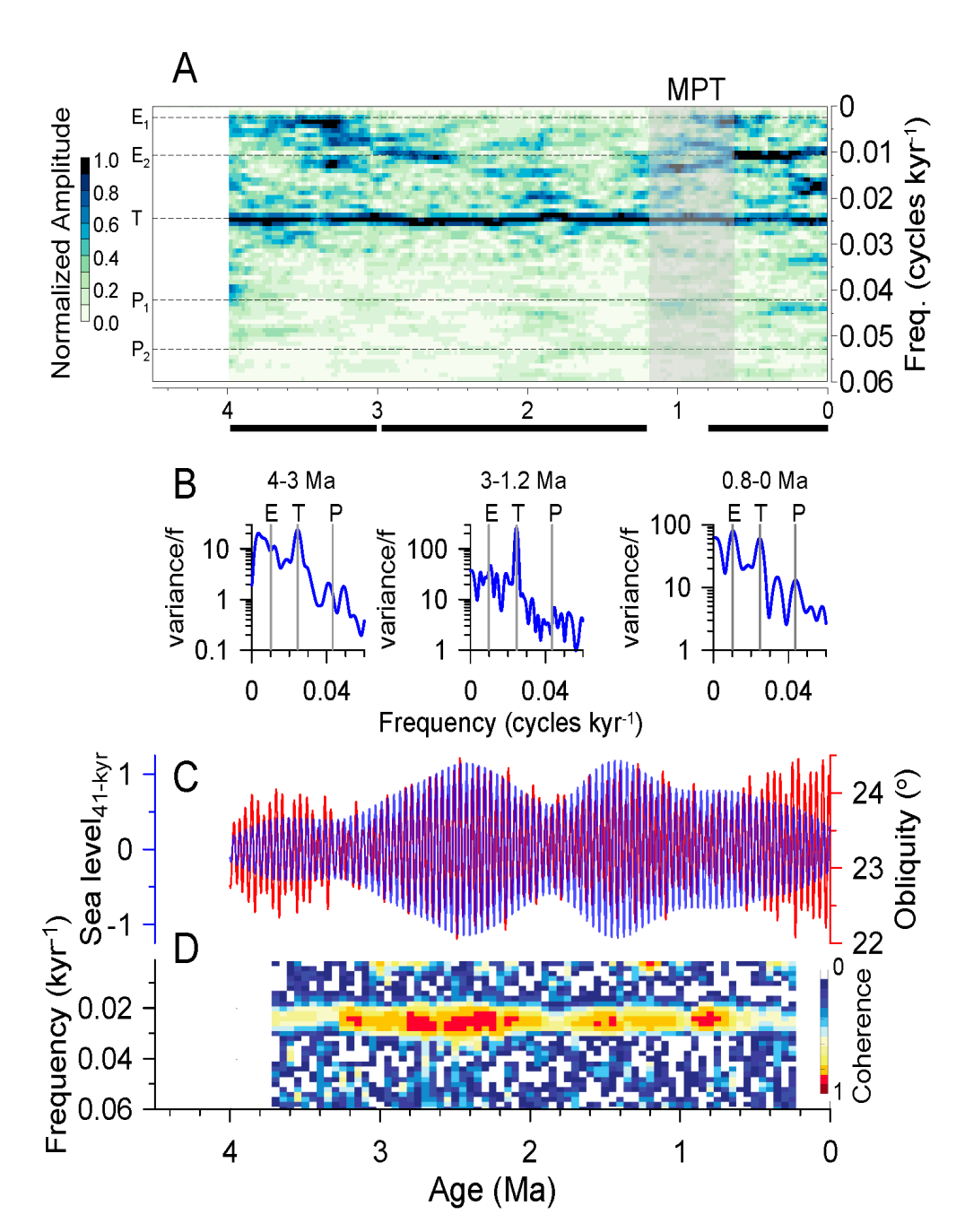


Fig. 2. Spectral characteristics of global mean sea level. (**A**) Evolutionary spectra of global mean sea level (GMSL). The dominant periods in insolation variations at orbital periods are indicated by horizontal lines (eccentricity: $E_1 = 400$ kyr, $E_2 = 96$ kyr; obliquity: T = 41 kyr and precession: $P_1 = 23$ kyr, $P_2 = 19$ kyr). Vertical gray rectangle represents the middle Pleistocene transition (MPT). (**B**) Spectral density of GMSL (variance per frequency) for three periods corresponding to horizontal black bars shown in (**A**) (3-4 Ma, 1.2-3 Ma, 0-0.8 Ma). Orbital periods are indicated by vertical lines (E = eccentricity (96 kyr), T = obliquity (41 kyr), and P = precession (23 kyr)). Note scale change for y-axes (variance/f). (**C**) Filtered GMSL using a 41-kyr filter (blue line) and obliquity (red line). (**D**) Coherence between 41-kyr filtered GMSL and obliquity.

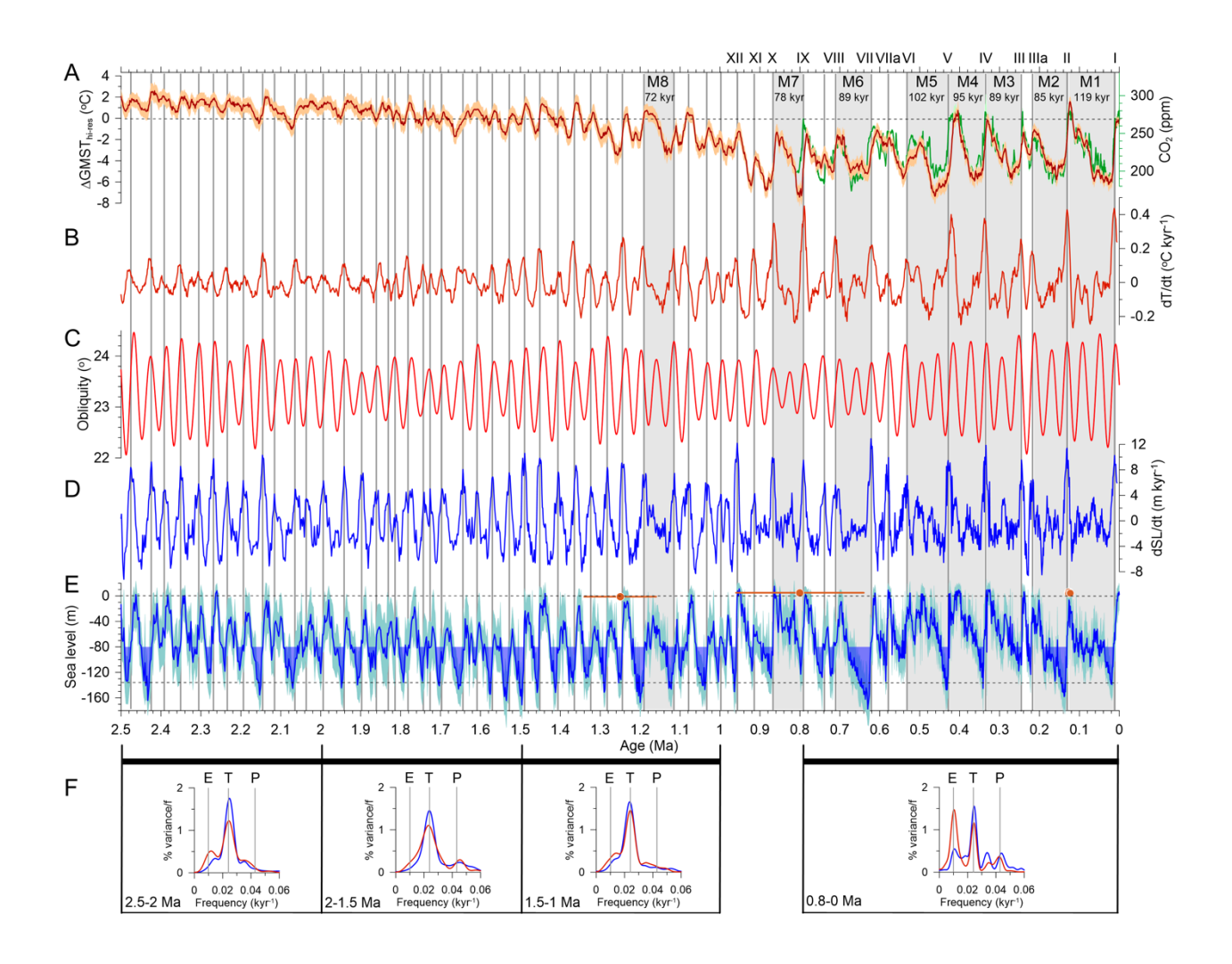


Fig. 3. Global temperature and sea-level changes over the past 2.5 Myr. (A) Global mean surface temperature change (Δ GMST) (brick red with 1 σ uncertainty,) referenced to PI, and atmospheric CO₂ (green) (122) placed on the AICC2023 chronology (123). (B) Rate of change of Δ GMST. (C) Obliquity (71). (D) Rate of change of global mean sea level (GMSL) (12-kyr running average), whose maxima are highlighted by vertical lines across (A-E). (E) Global mean sea level. Sea-level threshold of -80 m that, when exceeded, is followed by a termination upon next increase in obliquity (see text) is shown by filled blue sea-level intervals. Dashed horizontal lines correspond to present (0 m) and LGM (-130 m) sea levels. Brick-red symbols with 1 σ age uncertainty are published Pleistocene sea-level highstands (119, 120). (F) Spectral density of rate of change of Δ GMST (brick red) and GMSL (blue) for four periods corresponding to horizontal black bars shown in (E). Eccentricity (E, 100-kyr), tilt (T, 41-kyr) and precession (P, 23-kyr) frequency bands noted by vertical lines.

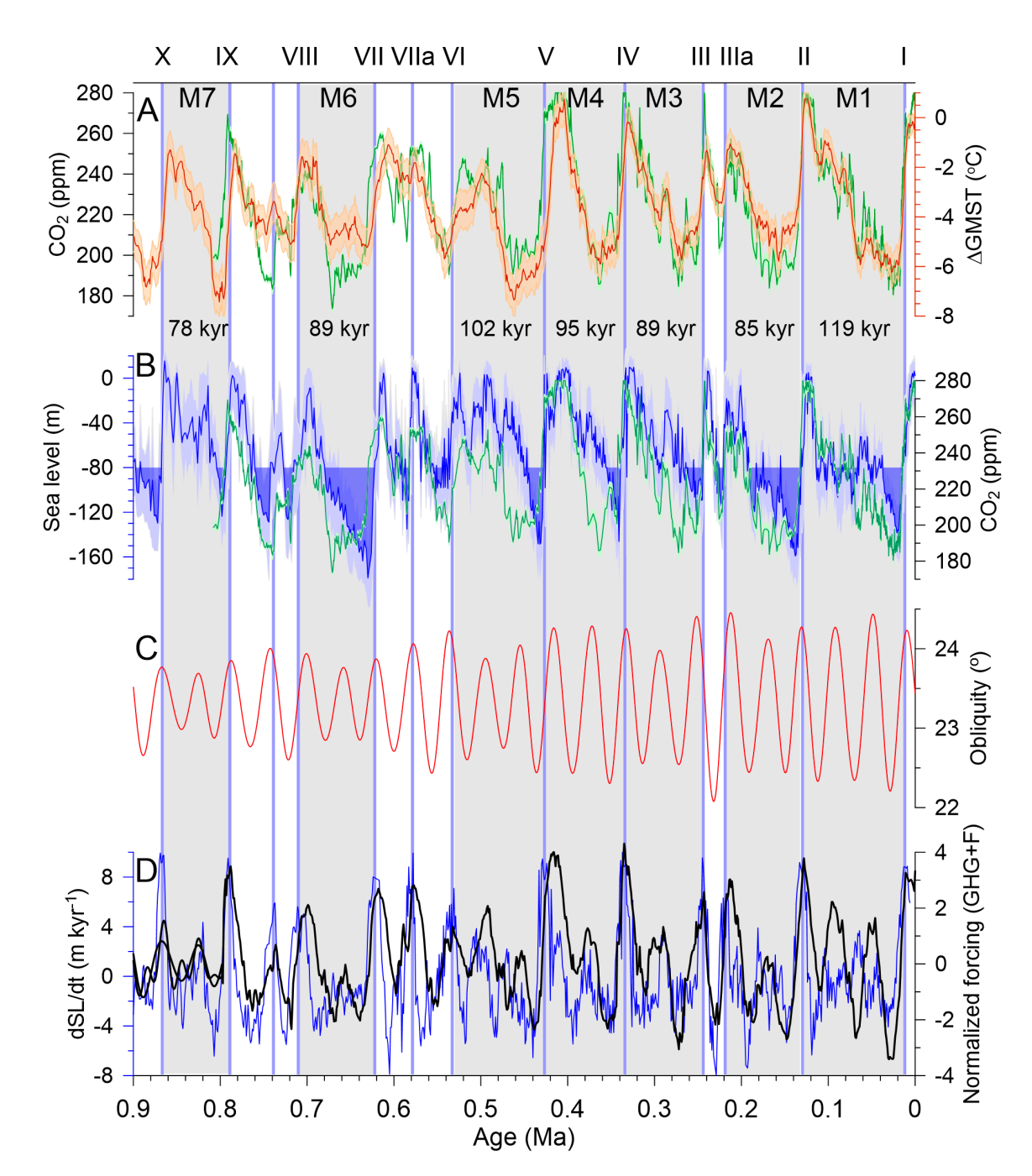


Fig. 4. Assessing the origin of the ~100-kyr cycle. (A) Global mean surface temperature change (Δ GMST) (brick red) referenced to PI, and atmospheric CO₂ (green) (122) both with 1σ uncertainty. (B) Global mean sea level (GMSL) (blue) and atmospheric CO₂ (green) (122), both with 1σ uncertainty. (C) Obliquity (71). (D) Rate of change of GMSL (blue) compared to a normalized forcing function F (GHG+F) (124) that combines normalized atmospheric CO₂ from the Antarctic ice-core record over the past 0.8 Myr (black) (122) placed on the AICC2023 chronology (123) and normalized obliquity. Note that there is no significant improvement in the correlation between rate of change of GMSL and a forcing function that combines various proportions of precession and obliquity (5:95, 25:75, 50:50).

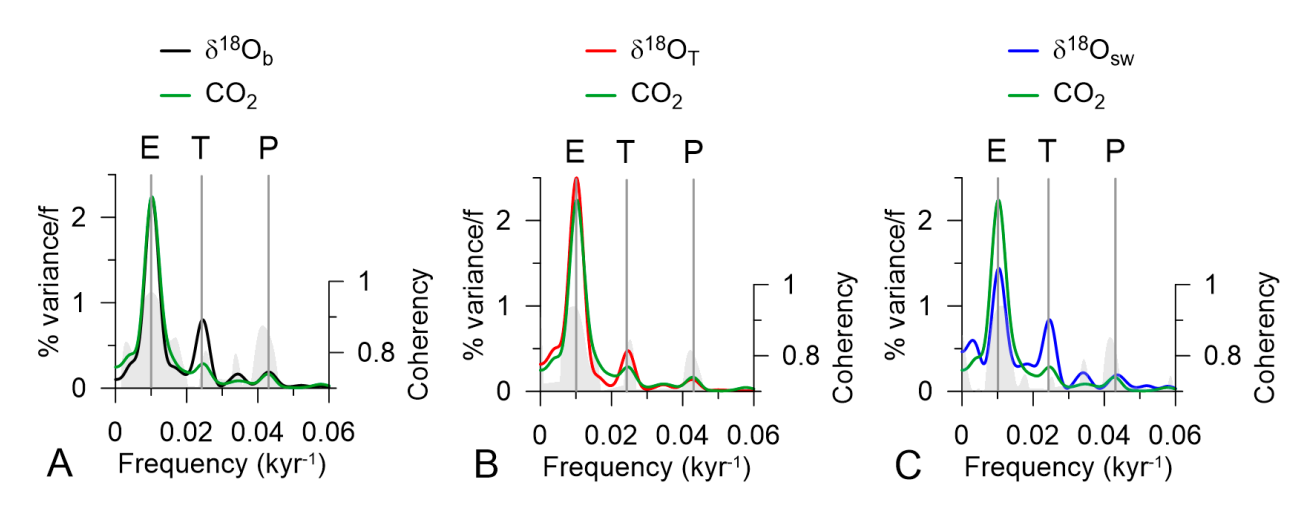


Fig. 5. Spectral density of the $\delta^{18}O_b$ record, its components, and atmospheric CO₂ for past 0.8 Myr. (A) Spectral density (normalized variance) of the Prob-stack $\delta^{18}O_b$ record (12) and atmospheric CO₂ (green) (122). (B) Spectral density (normalized variance) of the temperature component ($\delta^{18}O_T$) of the $\delta^{18}O_b$ record (18) and atmospheric CO₂ (green) (122). (C) Spectral density (normalized variance) of the seawater component ($\delta^{18}O_{sw}$) of the $\delta^{18}O_b$ record (18) and atmospheric CO₂ (green) (122)

REFERENCES AND NOTES

- 1. T. Westerhold *et al.*, An astronomically dated record of Earth's climate and its predictability over the last 66 million years. *Science* **369**, 1383-1387 (2020).
- 2. J. Zachos, M. Pagani, L. Sloan, E. Thomas, K. Billups, Trends, rhythms, and aberrations in global climate 65 Ma to present. *Science* **292**, 686-693 (2001).
- 3. N. J. Shackleton, N. D. Opdyke, R. M. Cline, J. D. Hays, Eds. (Geological Society of America Memoir, Boulder, CO, 1976), vol. 145, pp. 449-464.
- 4. N. G. Pisias, T. C. Moore, Jr., The evolution of Pleistocene climate: a time series approach. *Earth and Planetary Science Letters* **52**, 450-458 (1981).
- 5. P. U. Clark *et al.*, The middle Pleistocene transition: Characteristics. mechanisms, and implications for long-term changes in atmospheric PCO2. *Quaternary Science Reviews* **25**, 3150-3184 (2006).
- 6. J. D. Hays, J. Imbrie, N. J. Shackleton, Variations in the Earth's orbit: Pacemaker of the ice ages. *Science* **194**, 1121-1132 (1976).
- 7. J. Imbrie *et al.*, On the structure and origin of major glaciation cycles 1. Linear responses to Milankovitch forcing. *Paleoceanography* 7, 701-738 (1992).
- 8. J. Imbrie *et al.*, On the structure and origin of major glaciation cycles. 2. The 100,000-year cycle. *Paleoceanography* **8**, 699-735 (1993).
- 9. J. Hansen, M. Sato, G. Russell, P. Kharecha, Climate sensitivity, sea level and atmospheric carbon dioxide. *Philosophical Transactions of the Royal Society A-Mathematical Physical and Engineering Sciences* **371**, 10.1098/rsta.2012.0294 (2013).
- 10. N. G. Pisias *et al.*, High resolution stratigraphic correlation of benthic oxygen isotopic records spanning the last 300,000 years. *Marine Geology*, **56**, 119-136 (1984).
- 11. L. E. Lisiecki, M. E. Raymo, A Pliocene-Pleistocene stack of 57 globally distributed benthic δ¹⁸O records. *Paleoceanography* **20**, 2004PA001071 (2005).
- 12. S. Ahn, D. Khider, L. E. Lisiecki, C. E. Lawrence, A probabilistic Pliocene–Pleistocene stack of benthic δ^{18} O using a profile hidden Markov model. *Dynamics and Statistics of the Climate System* **2**, 1-16 (2017).
- 13. P. Huybers, Glacial variability over the last two million years: an extended depth-derived age model, continuous obliquity pacing, and the Pleistocene progression. *Quaternary Science Reviews* **26**, 37-55 (2007).
- 14. P. Bajo *et al.*, Persistent influence of obliquity on ice age terminations since the Middle Pleistocene transition. *Science* **367**, 1235-1239 (2020).
- M. E. Raymo, R. Kozdon, D. Evans, L. Lisiecki, H. L. Ford, The accuracy of mid-Pliocene δ¹8O-based ice volume and sea level reconstructions. *Earth-Science Reviews* 177, 291-302 (2018).
- 16. D. P. Schrag, Effects of diagenesis on the isotopic record of late Paleogene tropical sea surface temperatures. *Chemical Geology* **161**, 215-224 (1999).
- 17. H. J. Spero, J. Bijma, D. W. Lea, B. E. Bemis, Effect of seawater carbonate concentration on foraminiferal carbon and oxygen isotopes. *Nature* **390**, 497-500 (1997).
- 18. P. U. Clark *et al.*, Mean ocean temperature change and decomposition of the benthic δ 180 record over the past 4.5 million years. *Clim. Past* **21**, 973-1000 (2025).
- 19. M. J. Winnick, J. K. Caves, Oxygen isotope mass-balance constraints on Pliocene sea level and East Antarctic Ice Sheet stability. *Geology* **43**, 879-882 (2015).

- 20. E. Gasson, R. M. DeConto, D. Pollard, Modeling the oxygen isotope composition of the Antarctic ice sheet and its significance to Pliocene sea level. *Geology* **44**, 827-830 (2016).
- 21. P. U. Clark, J. D. Shakun, Y. Rosenthal, P. Köhler, P. J. Bartlein, Global and regional temperature change over the last 4.5 million years. *Science* **383**, 884-890 (2024).
- 22. K. G. Miller *et al.*, Cenozoic sea-level and cryospheric evolution from deep-sea geochemical and continental margin records. *Science Advances* **6**, eaaz1346 (2020).
- 23. J. D. Shakun, D. W. Lea, L. E. Lisiecki, M. E. Raymo, An 800-kyr record of global surface ocean delta O-18 and implications for ice volume-temperature coupling. *Earth and Planetary Science Letters* **426**, 58-68 (2015).
- 24. C. Waelbroeck *et al.*, Sea-level and deep water temperature changes derived from benthic foraminifera isotopic records. *Quaternary Science Reviews* **21**, 295-305 (2002).
- 25. S. L. Bates, M. Siddall, C. Waelbroeck, Hydrographic variations in deep ocean temperature over the mid-Pleistocene transition. *Quaternary Science Reviews* **88**, 147-158 (2014).
- 26. K. A. Jakob *et al.*, A new sea-level record for the Neogene/Quaternary boundary reveals transition to a more stable East Antarctic Ice Sheet. *Proceedings of the National Academy of Sciences of the United States of America* **117**, 30980-30987 (2020).
- 27. E. J. Rohling *et al.*, Comparison and synthesis of sea-level and deep-sea temperature variations over the past 40 million years. *Reviews of Geophysics* **60**, e2022RG000775 (2022).
- 28. E. J. Rohling *et al.*, Sea level and deep-sea temperature reconstructions suggest quasi-stable states and critical transitions over the past 40 million years. *Science Advances* 7, eabf5326 (2021).
- 29. P. R. Liautaud, D. A. Hodell, P. J. Huybers, Detection of significant climatic precession variability in early Pleistocene glacial cycles. *Earth and Planetary Science Letters* **536**, 116137 (2020).
- 30. S. Barker, L. E. Lisiecki, G. Knorr, S. Nuber, P. C. Tzedakis, Distinct roles for precession, obliquity, and eccentricity in Pleistocene 100-kyr glacial cycles. *Science* **387**, (2025).
- 31. P. Huybers, Early Pleistocene glacial cycles and the integrated summer insolation forcing. *Science* **313**, 508-511 (2006).
- 32. M. A. Maslin, X. S. Li, M. F. Loutre, A. Berger, The contribution of orbital forcing to the progressive intensification of Northern Hemisphere glaciation. *Quaternary Science Reviews* 17, 411-426 (1998).
- 33. H. Cheng *et al.*, Ice Age Terminations. *Science* **326**, 248-252 (2009).
- 34. H. Cheng *et al.*, The Asian monsoon over the past 640,000 years and ice age terminations. *Nature* **534**, 640-646 (2016).
- 35. P. C. Tzedakis, M. Crucifix, T. Mitsui, E. W. Wolff, A simple rule to determine which insolation cycles lead to interglacials. *Nature* **542**, 427-432 (2017).
- 36. P. Köhler, R. S. W. van de Wal, Interglacials of the Quaternary defined by northern hemispheric land ice distribution outside of Greenland. *Nature Communications* 11, 11:5124 (2020).
- 37. O. A. Dumitru *et al.*, Constraints on global mean sea level during Pliocene warmth. *Nature* **574**, 233-236 (2019).
- 38. K. G. Miller *et al.*, High tide of the warm Pliocene: Implications of global sea level for Antarctic deglaciation. *Geology* **40**, 407-410 (2012).
- 39. F. D. Richards *et al.*, Geodynamically corrected Pliocene shoreline elevations in Australia consistent with midrange projections of Antarctic ice loss. *Science Advances* **9**, (2023).

- 40. G. S. Dwyer, M. A. Chandler, Mid-Pliocene sea level and continental ice volume based on coupled benthic Mg/Ca palaeotemperatures and oxygen isotopes. *Philosophical Transactions of the Royal Society A-Mathematical Physical and Engineering Sciences* **367**, 157-168 (2009).
- 41. S. Sosdian, Y. Rosenthal, Deep-sea temperature and ice volume changes across the Pliocene-Pleistocene climate transitions. *Science* **325**, 306-310 (2009).
- 42. G. Balco, C. W. Rovey, Absolute chronology for major Pleistocene advances of the Laurentide Ice Sheet. *Geology* **38**, 795-798 (2010).
- 43. A. J. Hidy, J. C. Gosse, D. G. Froese, J. D. Bond, D. H. Rood, A latest Pliocene age for the earliest and most extensive Cordilleran Ice Sheet in northwestern Canada. *Quaternary Science Reviews* **61**, 77-84 (2013).
- 44. J. D. Shakun, M. E. Raymo, D. W. Lea, An early Pleistocene Mg/Ca-δ¹⁸O record from the Gulf of Mexico: Evaluating ice sheet size and pacing in the 41-kyr world. *Paleoceanography* **31**, 1011-1027 (2016).
- 45. K. Blake-Mizen *et al.*, Southern Greenland glaciation and Western Boundary Undercurrent evolution recorded on Eirik Drift during the late Pliocene intensification of Northern Hemisphere glaciation. *Quaternary Science Reviews* **209**, 40-51 (2019).
- 46. B. R. Rea *et al.*, Extensive marine-terminating ice sheets in Europe from 2.5 million years ago. *Science Advances* **4**, eaar8327 (2018).
- 47. E. Jansen, T. Fronval, F. Rack, J. E. T. Channell, Pliocene-Pleistocene ice rafting history and cyclicity in the Nordic Seas during the last 3.5 Myr. *Paleoceanography* **15**, 709-721 (2000).
- 48. G. H. Haug, D. M. Sigman, R. Tiedemann, T. F. Pedersen, M. Sarnthein, Onset of permanent stratification in the subarctic Pacific Ocean. *Nature* **401**, 779-782 (1999).
- 49. N. J. Shackleton, N. D. Opdyke, Oxygen isotope and paleomagnetic evidence for early Northern Hemisphere glaciation. *Nature* **270**, 216-219 (1977).
- 50. M. E. Raymo, The initiation of Northern Hemisphere glaciation. *Annual Review of Earth Planetary Sciences*, **22**, 353-383 (1994).
- 51. P. U. Clark, D. Pollard, Origin of the middle Pleistocene transition by ice sheet erosion of regolith. *Paleoceanography* **13**, 1-9 (1998).
- 52. M. E. Raymo, K. Nisancioglu, The 41 kyr world: Milankovitch's other unsolved mystery. *Paleoceanography* **18**, 2002PA000791 (2003).
- 53. P. Huybers, E. Tziperman, Integrated summer insolation forcing and 40,000-year glacial cycles: The perspective from an ice-sheet/energy-balance model. *Paleoceanography* 23, PA1208 (2008).
- 54. C. R. Tabor, C. J. Poulsen, D. Pollard, How obliquity cycles powered early Pleistocene global ice-volume variability. *Geophysical Research Letters* **42**, 1871-1879 (2015).
- J. Boellstorff, North American Pleistocene stages reconsidered in light of probably Pliocene-Pleistocene continental glaciation. *Science* **202**, 305-307 (1978).
- 56. M. E. Raymo, L. E. Lisiecki, K. H. Nisancioglu, Plio-Pleistocene ice volume, Antarctic climate, and the global delta O-18 record. *Science* **313**, 492-495 (2006).
- 57. K. A. Dyez, B. Honisch, G. A. Schmidt, Early Pleistocene Obliquity-Scale pCO(2) Variability at similar to 1.5 Million Years Ago. *Paleoceanography and Paleoclimatology* 33, 1270-1291 (2018).
- 58. Z. Liu, H. Yang, Extratropical control of tropical climate, the atmospheric bridge and oceanic tunnel. *Geophysical Research Letters* **30**, 1230 (2003).

- 59. S. Y. Lee, C. J. Poulsen, Sea ice control of Plio-Pleistocene tropical Pacific climate evolution. *Earth and Planetary Science Letters* **248**, 253-262 (2006).
- 60. T. D. Herbert, L. C. Peterson, K. T. Lawrence, Z. Liu, Tropical ocean temperatures over the past 3.5 million years. *Science* **328**, 1530-1534 (2010).
- 61. P. Huybers, P. Molnar, Tropical cooling and the onset of North American glaciation. *Climate of the Past* **3**, 549-557 (2007).
- 62. P. U. Clark, S. W. Hostetler, N. G. Pisias, A. Schmittner, K. J. Meissner, in *Ocean Circulation: Mechanisms and Impacts*, A. Schmittner, J. Chiang, S. Hemming, Eds. (American Geophysical Union, Geophysical Monograph, 2007), vol. 173, pp. 209-246.
- 63. M. P. Erb, C. S. Jackson, A. J. Broccoli, Using Single-Forcing GCM Simulations to Reconstruct and Interpret Quaternary Climate Change. *Journal of Climate* **28**, 9746-9767 (2015).
- 64. J. Fyke, O. Sergienko, M. Lofverstrom, S. Price, J. T. M. Lenaerts, An overview of interactions and feedbacks between ice sheets and the Earth system. *Reviews of Geophysics* **56**, 361-408 (2018).
- 65. X. Li *et al.*, Mid-Pliocene westerlies from PlioMIP simulations. *Advances in Atmospheric Sciences* **32**, 909-923 (2015).
- 66. S. Hofer, A. J. Tedstone, X. Fettweis, J. L. Bamber, Decreasing cloud cover drives the recent mass loss on the Greenland Ice Sheet. *Science Advances* **3**, e1700584 (2017).
- 67. N. Sagoo *et al.*, Observationally constrained cloud phase unmasks orbitally driven climate feedbacks. *Geophysical Research Letters* **48**, e2020GL091873 (2021).
- 68. N. Unger, X. Yue, Strong chemistry- climate feedbacks in the Pliocene. *Geophysical Research Letters* **41**, 527-533 (2014).
- 69. D. Pollard, S. L. Thompson, Climate and ice-sheet mass balance at the Last Glacial Maximum from GENESIS version 2 global climate model. *Quaternary Science Reviews* **16**, 841-863 (1997).
- 70. S. L. Thompson, D. Pollard, Greenland and Antarctic mass balances for present and doubled atmospheric CO2 from the GENESIS version-2 global climate model. *Journal of Climate* **10**, 871-900 (1997).
- 71. J. Laskar *et al.*, A long term numerical solution for the insolation quantities of the Earth. *Astronomy and Astrophysics* **428**, 261-285 (2004).
- 72. P. Köhler, Atmospheric CO₂ concentration based on boron isotopes versus simulations of the global carbon cycle during the Plio-Pleistocene. *Paleoceanography and Paleoclimatology* **38**, e2022PA004439 (2023).
- 73. A. Berger, X. S. Li, M. F. Loutre, Modelling northern hemisphere ice volume over the last 3 Ma. *Quaternary Science Reviews* **18**, 1-11 (1999).
- 74. M. Willeit, A. Ganopolski, R. Calov, V. Brovkin, Mid-Pleistocene transition in glacial cycles explained by declining CO₂ and regolith removal. *Science Advances* 5, eaav7337 (2019).
- 75. E. Tziperman, H. Gildor, On the mid-Pleistocene transition to 100-kyr glacial cycles and the asymmetry between glaciation and deglaciation times. *Paleoceanography* 18, PA000627 (2003).
- 76. P. Huybers, C. Wunsch, Obliquity pacing of the late Pleistocene glacial terminations. *Nature* **434**, 491-494 (2005).
- 77. T. B. Chalk *et al.*, Causes of ice age intensification across the Mid-Pleistocene Transition. *Proceedings of the National Academy of Sciences* **114**, 13114-13119 (2017).

- 78. N. J. Shackleton, The 100,000 year Ice-Age cycle identified and found to lag temperature, carbon dioxides and orbital eccentricity. *Science* **289**, 1897-1902 (2000).
- 79. J. Imbrie, J. Z. Imbrie, Modeling the climatic response to orbital variations. *Science* **207**, 943-953 (1980).
- 80. A. Abe-Ouchi *et al.*, Insolation-driven 100,000-year glacial cycles and hysteresis of ice-sheet volume. *Nature* **500**, 190-193 (2013).
- 81. D. Pollard, A simple ice sheet model yields realistic 100 kyr glacial cycles. *Nature* **296**, 334-338 (1982).
- 82. P. U. Clark, R. B. Alley, D. Pollard, Northern Hemisphere ice-sheet influences on global climate change. *Science* **286**, 1104-1111 (1999).
- 83. W. F. Ruddiman, M. E. Raymo, D. G. Martinson, B. M. Clement, J. Backman, Pleistocene evolution: northern hemisphere ice sheets and North Atlantic ocean. *Paleoceanography* 4, 353-412 (1989).
- 84. D. M. Sigman *et al.*, The Southern Ocean during the ice ages: A review of the Antarctic surface isolation hypothesis, with comparison to the North Pacific. *Quaternary Science Reviews* **254**, 106732 (2021).
- 85. A. Martinez-Garcia *et al.*, Southern Ocean dust-climate coupling over the past four million years. *Nature* **476**, 312-315 (2011).
- 86. A. P. Hasenfratz *et al.*, The residence time of Southern Ocean surface waters and the 100,000-year ice age cycle. *Science* **363**, 1080-1084 (2019).
- 87. R. Ferrari *et al.*, Antarctic sea ice control on ocean circulation in present and glacial climates. *Proceedings of the National Academy of Sciences* **111**, 8753-8758 (2014).
- 88. M. F. Jansen, Glacial ocean circulation and stratification explained by reduced atmospheric temperature. *Proceedings of the National Academy of Sciences* **114**, 45-50 (2017).
- 89. A. Marzocchi, M. F. Jansen, Global cooling linked to increased glacial carbon storage via changes in Antarctic sea ice. *Nature Geoscience* **12**, 1001-1005 (2019).
- 90. P. Köhler, R. Bintanja, The carbon cycle during the Mid Pleistocene Transition: the Southern Ocean decoupling hypothesis. *Climate of the Past* **4**, 311-332 (2008).
- 91. D. Pollard, A coupled climate-ice sheet model applied to the Quaternary ice ages. *Journal of Geophysical Research* **88**, 7705-7718 (1983).
- 92. S. J. Marshall, P. U. Clark, Basal temperature evolution of North American ice sheets and implications for the 100-kyr cycle. *Geophysical Research Letters* **29**, GL015192 (2002).
- 93. P. U. Clark *et al.*, Oceanic forcing of penultimate deglacial and last interglacial sea-level rise. *Nature* **577**, 660-664 (2020).
- 94. M. E. Raymo, The timing of major climate terminations. *Paleoceanography* **12**, 577-585 (1997).
- 95. W. S. Broecker, J. van Donk, Insolation changes, ice volumes, and the O-18 record in deep-sea cores. *Reviews of Geophysics and Space Physics* **8**, 169-198 (1970).
- 96. N. J. Shackleton, The oxygen isotope stratigraphic record of the Late Pleistocene. *Philosophical Transactions Royal Society of London* **280B**, 169-182 (1977).
- 97. S. Barker *et al.*, Persistent influence of precession on northern ice sheet variability since the early Pleistocene. *Science* **376**, 961-967 (2022).
- 98. M. Siddall, B. Honisch, C. Waelbroeck, P. Huybers, Changes in deep Pacific temperature during the mid-Pleistocene transition and Quaternary. *Quaternary Science Reviews* **29**, 170-181 (2010).

- 99. R. M. Spratt, L. E. Lisiecki, A Late Pleistocene sea level stack. *Climate of the Past* 12, 1079-1092 (2016).
- 100. J. E. Hansen *et al.*, Global warming in the pipeline. *Oxford Open Climate Change* **3**, kgad008 (2023).
- 101. H. Elderfield *et al.*, Evolution of ocean temperature and ice volume through the mid-Pleistocene climate transition. *Science* **337**, 704-709 (2012).
- 102. S. C. Woodard *et al.*, Antarctic role in Northern Hemisphere glaciation. *Science* **346**, 847-851 (2014).
- 103. H. L. Ford, M. E. Raymo, Regional and global signals in seawater δ^{18} O records across the mid-Pleistocene transition. *Geology* **48**, 113-117 (2020).
- 104. A. C. Mix, W. F. Ruddiman, Oxygen-isotope analyses and Pleistocene ice volumes. *Quaternary Research* **21**, 1-20 (1984).
- 105. G. R. Grant *et al.*, Reduced magnitude of Early Pleistocene intensification of Northern Hemisphere Glaciation. *Quaternary Science Reviews* **349**, 109096 (2025).
- 106. G. R. Grant *et al.*, The amplitude and origin of sea-level variability during the Pliocene epoch. *Nature* **574**, 237-241 (2019).
- 107. D. P. Schrag *et al.*, The oxygen isotopic composition of seawater during the Last Glacial Maximum. *Quaternary Science Reviews* **21**, 331-342 (2002).
- 108. K. Lambeck, H. Rouby, A. Purcell, Y. Sun, M. Sambridge, Sea level and global ice volumes from the Last Glacial Maximum to the Holocene. *Proceedings of the National Academy of Sciences* **111**, 15296-15303 (2014).
- 109. M. B. Priestley, Evolutionary spectra and non-stationary processes. *Journal of the Royal Statistical Society, Series B* **27**, 204-237 (1965).
- 110. S. R. Meyers. (https://cran.r-project.org/package=astrochron, 2014).
- 111. C. T. R, in *R Foundation for Statistical Computing*. (Vienna, Austria, 2024).
- 112. D. J. Thomson, Spectrum estimation and harmonic analysis. *Proceedings of the IEEE* **70**, 1055-1096 (1982).
- 113. S. Developers. (https://CRAN.R-project.org/package=signal, 2013).
- 114. P. Howell, N. Pisias, J. Ballance, J. Baughman, L. Ochs, ARAND Time-Series Analysis Software. (2006).
- 115. I. Janssens, P. Huybrechts, The Treatment of Meltwater Retardation in Mass-Balance Parameterizations of the Greenland Ice Sheet. *Annals of Glaciology* **31**, 133-140 (2000).
- 116. B. Honisch, N. G. Hemming, D. Archer, M. Siddall, J. F. McManus, Atmospheric Carbon Dioxide Concentration Across the Mid-Pleistocene Transition. *Science* **324**, 1551-1554 (2009).
- 117. G. Bartoli, B. Honisch, R. E. Zeebe, Atmospheric CO2 decline during the Pliocene intensification of Northern Hemisphere glaciations. *Paleoceanography* **26**, (2011).
- 118. L. Tarasov, A. S. Dyke, R. M. Neal, W. R. Peltier, A data-calibrated distribution of deglacial chronologies for the North American ice complex from glaciological modeling. *Earth and Planetary Science Letters* **315**, 30-40 (2012).
- 119. O. A. Dumitru *et al.*, Sea-level stands from the Western Mediterranean over the past 6.5 million years. *Sci Rep-Uk* **11**, 6681 (2021).
- 120. A. Dutton, J. M. Webster, D. Zwartz, K. Lambeck, B. Wohlfarth, Tropical tales of polar ice: evidence of Last Interglacial polar ice sheet retreat recorded by fossil reefs of the granitic Seychelles islands. *Quaternary Science Reviews* **107**, 182-196 (2015).

- 121. D. Ottesen, C. L. Batchelor, H. Loseth, H. Brunstad, 3D seismic evidence for a single Early Pleistocene glaciation of the central North Sea. *Science Advances* **10**, eadq6089 (2024).
- 122. B. Bereiter *et al.*, Revision of the EPICA Dome C CO₂ record from 800 to 600kyr before present. *Geophysical Research Letters* **42**, 542-549 (2015).
- 123. M. Bouchet *et al.*, The Antarctic Ice Core Chronology 2023 (AICC2023) chronological framework and associated timescale for the European Project for Ice Coring in Antarctica (EPICA) Dome C ice core. *Clim. Past* **19**, 2257-2286 (2023).
- 124. P. Huybers, Combined obliquity and precession pacing of late Pleistocene deglaciations. *Nature* **480**, 229-232 (2011).
- 125. N. Lhomme, G. K. C. Clarke, C. Ritz, Global budget of water isotopes inferred from polar ice sheets. *Geophysical Research Letters* **32**, L20502 (2005).
- 126. A. Sima, A. Paul, M. Schulz, J. Oerlemans, Modeling the oxygen-isotopic composition of the North American Ice Sheet and its effect on the isotopic composition of the ocean during the last glacial cycle. *Geophysical Research Letters* **33**, L15706 (2006).
- 127. T. Tharammal, A. Paul, U. Merkel, D. Noone, Influence of Last Glacial Maximum boundary conditions on the global water isotope distribution in an atmospheric general circulation model. *Climate of the Past* **9**, 789-809 (2013).
- 128. R. M. DeConto, D. Pollard, Contribution of Antarctica to past and future sea-level rise. *Nature* **531**, 591-597 (2016).
- 129. W. R. Peltier, D. F. Argus, R. Drummond, Space geodesy constrains ice age terminal deglaciation: The global ICE-6G_C (VM5a) model. *Journal of Geophysical Research-Solid Earth* **120**, 450-487 (2015).
- 130. K. M. Grant *et al.*, Sea-level variability over five glacial cycles. *Nature Communications* 5, 5076 (2014).
- 131. Y. Yokoyama *et al.*, Rapid glaciation and a two-step sea level plunge into the Last Glacial Maximum. *Nature* **559**, 603-607 (2018).

Acknowledgments: This publication contributed to Beyond EPICA, a project of the European

Union's Horizon 2020 research and innovation program (Oldest Ice Core). This is Beyond EPICA

publication number 45.

Funding:

National Science Foundation OPP-2103032 (PUC)

University of Oregon Fund for Faculty Excellence (PB)

National Science Foundation OCE-1810681 (ZL)

National Science Foundation OCE-1834208 (YR)

Author contributions:

Conceptualization: PUC, JDS

Methodology: JDS, YR, DP, SWH, PUC, PJB, NGP

Investigation: PUC, JDS, YR, DP, SWH, PK, PJB

Writing – original draft: PUC

Writing – review & editing: PUC, JDS, YR, DP, SWH, PK, PJB, JMG, DPS, CZ, ZL, NGP

Competing interests: Authors declare that they have no competing interests.

Data Availability Statement: All data are available in the Supplementary Material.

Supplementary Materials

Equations and parameters to convert $\delta^{18}O_{sw}$ to sea level

Figs. S1 to S10

Table S1

References (125-131)

35